DC Power Boosting Circuit for Freestanding-Sliding Triboelectric Nanogenerators with High Intrinsic Impedance and Multi-Harmonic Output

Kibae Lee[1], Ji-Seok Kim[2], Saewoong Oh[2], Hyunjoon Yoo[2], Jongkil Lee[3], Il -Kwon Oh[2], and Chong Hyun Lee[1]

[1]Jeju National University
[2]Korea Advanced Institute of Science and Technology
[3]Andong National University

June 13, 2023

Abstract

This study proposes a direct current power supply circuit (DPS) that can match the impedance of the freestanding-sliding mode triboelectric nanogenerator (FS-TENG) with multi-harmonic characteristics and continuously supply power to the load with reduced energy loss. The proposed DPS consists of a double charge circuit (DCC) and a DC conversion circuit based on a comb filtering circuit (CFC). The proposed DPS successfully matched the high internal impedance of the FS-TENG, collected multi-harmonic electrical energy, and provided stable DC voltage for practical applications in real-time. The proposed FS-TENG and DPS supplied a continuous DC voltage of 2.2 V to loads with 0.039 % ripple, while reducing the impedance of the TENG from 221 MΩ to 11 MΩ. The present results demonstrate that the proposed DPS has higher output power than conventional buck and buck-boost converters for the FS-TENG with high impedance and multi-harmonic characteristics. This work presents a significant advancement towards continuous DC power supply utilizing the FS-TENG. In addition, the practical application of the FS-TENG and DPS was successfully demonstrated to drive a self-powered temperature sensor in real-time by generating a constant DC output voltage across a thermistor.

Keywords: *triboeletric nanogenerators; multi-harmonic output signals; DC power supply circuit; freestanding-sliding mode; interdigitated electrodes;*

Abstract

This study proposes a direct current power supply circuit (DPS) that can match the impedance of the freestanding-sliding mode triboelectric nanogenerator (FS-TENG) with multi-harmonic characteristics and continuously supply power to the load with reduced energy loss. The proposed DPS consists of a double charge circuit (DCC) and a DC conversion circuit based on a comb filtering circuit (CFC). The proposed DPS successfully matched the high internal impedance of the FS-TENG, collected multi-harmonic electrical energy, and provided stable DC voltage for practical applications in real-time. The proposed FS-TENG and DPS supplied a continuous DC voltage of 2.2 V to loads with 0.039 % ripple, while reducing the impedance of the TENG from 221 MΩ to 11 MΩ. The present results demonstrate that the proposed DPS has higher output power than conventional buck and buck-boost converters for the FS-TENG with high impedance and multi-harmonic characteristics. This work presents a significant advancement towards continuous DC power supply utilizing the FS-TENG. In addition, the practical application of the FS-TENG and DPS was successfully demonstrated to drive a self-powered temperature sensor in real-time by generating a constant DC output voltage across a thermistor.

1. Introduction

The increasing concern about energy deficiency and environmental pollution has led to the development of environment-friendly renewable energy harvesting technology.[1, 2] For the realization of renewable energy to harness the vast amounts of wasted mechanical energy, there has been a significant increase in interest in sustainable and mass-producible mechanical energy harvesters that can convert wasted energy into electricity.[3, 4] Triboelectric nanogenerators (TENGs) have gained great attention as a promising energy harvesting technology due to their advantages such as scalability, light weight, easy fabrication method, high degree of freedom in material selection, and high efficiency in low-frequency motion.[5-9] TENGs generate electricity by utilizing wasted mechanical energy based on a synergetic effect of triboelectrification and electrostatic induction to maintain electrostatic equilibrium.[10, 11] TENGs mainly have several distinguishable operating modes for different types of mechanical motion: vertical contact-separation mode,[12] lateral sliding mode,[13] single electrode mode,[14] and freestanding-sliding mode[15].

Among the various operating modes, the freestanding-sliding mode TENG (FS-TENG) can be easily applied because the slider as a moving part has no connection for the electrical wire, which enables stable operation.[16-18] In addition, the root-mean-square (RMS) value of the output voltage signal can be improved through frequency multiplication even with the same input movement by using an appropriate number of interdigitated electrodes for the number of segments.[19, 20] In addition, this type of frequency multiplication has been strategically utilized to harvest wasted mechanical motion, especially in the low-frequency band, because the output current can also be enhanced as the electron transfer rate between the two interdigitated electrodes increases.[19] Therefore, FS-TENGs with interdigitated electrodes have been proposed to convert low-frequency wasted mechanical energy into electrical energy in several mechanical motions such as water droplets[21], ocean waves[22], and biomechanical motions[23, 24]. Thus, interdigitated electrodes improve energy harvesting efficiency by increasing the output frequency compared to the input frequency, which is known as the frequency up-conversion mechanism.[19]

However, the high internal impedance resulting from the physical gap between the interdigitated electrodes in the FS-TENG causes energy leakage during the power transfer process.[25, 26] To reduce the energy leakage due to the high impedance property of the TENG, various methods have been proposed, including storing the rectified energy and supplying power through switching operation and DC/DC conversion.[27, 28] Ahn *et al* . proposed an impedance coupler switching a bridge diode rectifier and an electrical load,[27] while Liang *et al* . proposed a charge excitation circuit (CEC) using capacitors and MOSFET transistors.[28] The CEC played a crucial role in increasing the capacitance of the TENG to match the impedance and switching two capacitors from parallel to series connection to charge the doubled voltage. However, the proposed methods are not suitable for continuous power supply due to the minimum charging time required and the intermittent power transfer. More importantly, the output signals of higher order harmonics are not properly collected, resulting in higher energy loss, which is another critical issue in interdigitated electrode FS-TENGs. Therefore, the development of a power boost circuit for interdigitated electrode FS-TENGs is highly required to overcome two major energy loss problems and enable continuous power supply by converting low-frequency wasted mechanical energy.

In this context, several approaches have been proposed to boost the power transfer efficiency. One such approach involves using an impedance matching circuit based on transformers, along with a DC power supply circuit featuring bridge diodes and capacitor banks.[29] However, this method had some practical limitations since it operates at high frequencies of several kHz, and requires a large custom transformer. Another method involves using a DC buck converter circuit for the continuous power supply, which was proposed by Xi *et al* .[30] However, the use of this circuit is limited in specific TENGs which can generate a constant peak voltage to a certain extent, owing to the fixed threshold voltage of the comparator used for switch control.

Herein, this study proposes a DC power supply circuit (DPS) that enables continuous power supply to the load while matching the impedance of the FS-TENG. The proposed DPS utilizes a double charge circuit (DCC) comprising capacitors and metal-oxide-semiconductor field-effect transistors (MOSFETs), and a DC

conversion circuit based on a comb filtering circuit (CFC) employing resistor, inductor, and capacitor (RLC) devices. The proposed DPS successfully addresses the high impedance of the FS-TENG, and collects multi-halmonic electrical energy to deliver a stable DC voltage for real-time practical applications. This work investigates the multi-harmonic output of the variable slider contact areas in the interdigitated electrode FS-TENG, and proposes a power management circuit for the FS-TENG with multi-harmonic output signals for the first time. Moreover, the proposed DPS shows superior output power compared to conventional buck and buck-boost converters for the FS-TENG with high impedance and multi-harmonic characteristics. Our findings demonstrate that the proposed FS-TENG and DPS can supply continuous DC voltage of 2.2 V to loads while reducing the TENG impedance from 221 MΩ to 11 MΩ. Notably, this work provides a DC output voltage of 2.2 V at the extremely low sliding frequency of 0.625 Hz. We believe this study contributes significantly to the development of energy harvesting devices and energy conversion circuits by addressing the high impedance and multi-harmonic signal collection, and thus paving the way for the practical applications of FS-TENGs.

2. Results and Discussion

The FS-TENG used for harvesting energy in this paper is schematically illustrated in **Figure 1a** . The FS-TENG consists of a stator part with interdigitated electrodes and a sliding part with a freestanding slider. The copper interdigitated electrodes are attached to the acrylic substrate for the stator and they are fully covered by polytetrafluoroethylene (PTFE) film as an electronegative triboelectric material. In the freestanding-sliding part, a ladder-shaped copper film acts as a relatively electropositive triboelectric material compared to the PTFE film and there is no need to connect the electrical wire to the copper film on the freestanding-sliding part. **Figure 1b** shows the reciprocating sliding motion of the suggested FS-TENG; the freestanding slider moves from the left limit (i) to the right limit (ii) keeping in contact with the PTFE film for friction.

The operating mechanism of the FS-TENG is based on a coupling effect of triboelectrification and electrostatic induction as schematically illustrated in **Figure 1c** .[10] The physical contact and frictional force between the copper film in the freestanding slider and the PTFE film in the stator induce triboelectrification effects on both the copper film and the PTFE film, with opposite charges, positive and negative, respectively. Notably, the charge density of the copper film is twice that of the PTFE film due to the charge equilibrium because the contact area of the copper film is half that of the PTFE film.[15, 19, 31] The interdigitated copper electrodes are charged with opposite signs because of the electrostatic induction effect used to maintain the charge equilibrium (i). When the freestanding slider slides slightly and moves on the PTFE film toward the right, electrostatically induced charges in the copper interdigitated electrodes change as the electron moves between the two electrodes in a short-circuit condition (ii); after that, when the freestanding slider reaches the next interdigitated electrodes, opposite charges (compared to the initial state) are induced in both copper interdigitated electrodes (iii). Thereafter, the electrons flow in the opposite direction of (ii) when the freestanding slider moves further (iv). Finally, one reciprocating process of charge transfer between the two electrodes is over when the freestanding slider reaches the same electrode in the initial state (v). The proposed FS-TENG uses a frequency up-conversion effect to multiply the output frequency in proportion to the number of segments in the FS-TENG (N), with a constant sliding speed because the AC output signal is generated following the aforementioned operation mechanism.[32, 33]

Figure 1d–e show the circuit diagram of the proposed DPS and the AC/DC power conversion process of signals generated by the FS-TENG. The proposed DPS is composed of DCC and CFC to supply power to the load. The DCC charges the power of the differential signal generated by the FS-TENG to the capacitor by means of switching operation using P-type and N-type MOSFET transistors. The DCC serves to rectify the negative voltage generated by the FS-TENG into a positive voltage. Meanwhile, in order to effectively collect the multi-harmonic electrical energy emanating from the interdigitated electrode FS-TENG, the CFC employs a multi-harmonic resonance targeting RLC filter circuit. As a result, the electrical energy characterized by the aforementioned multi-harmonic components, which is supplied by the FS-TENG, can be collected with high efficiency, and a constant DC voltage can be directly supplied directly to the load as

shown in **Figure 1e** .

For the electrical characterization of the FS-TENG, a series of experiments were conducted to measure the output voltages. Sepecifically, a motorized linear stage was employed to control the sliding speeds. The structure and motion of the FS-TENG are illustrated in **Figures 2a–b** , which depict the forward and backward motion direction, respectively. To investigate the effect of N in the design of the interdigitated electrodes, a methodical design approach was utilized to achieve varying N values while maintaining a constant total length (L) and width (w), as shown in**Figure S1** . As the value of N increased in the design of the interdigitated electrodes, the length of each electrode (l) and the interelectrode gap (g) were gradually reduced. The specific parameters associated with each N used in the experiments can be found in **Table S1** . The FS-TENGs fabricated with different values of N values are shown in **Figure S2** . To enable an effective comparison of the characteristics of output voltages (V) of the FS-TENGs with different values of N values, measurements were conducted at the same sliding speed of 100 mm/s and plotted in normalized form, divided by the maximum voltage (V_{max}) for clear comparison, as shown in**Figure 2c** . As the value of N increased, the frequency of the output voltage also increased proportionally owing to the reduced time required to generate a single AC signal resulting from the decreased distance between the interdigitated electrodes. Next, we conducted experiments to investigate the effect of sliding speed on the output voltage. **Figures 2d–f** provide the output voltages of FS-TENGs with varying N values, specifically 4, 6, and 8, respectively, at different sliding speeds during a single reciprocating motion. The results indicate that the output voltage generated by FS-TENG is dependent on the sliding speed; a higher output voltage was observed at faster sliding speeds using the same FS-TENG. The output signals obtained at different sliding speeds were transformed into spectral components, thereby enabling the extraction of frequency information of the signals to accurately identify the harmonic output signals of the FS-TENGs.

Figures 2g–i depict the power spectra of the output signals of the FS-TENGs at sliding speeds of 100 mm/s, 200 mm/s, and 300 mm/s, respectively. These power spectra show dominant peaks of harmonic output signals and reveal the correlation between harmonic frequencies at the same speed. It is noteworthy that as the sliding speed increases, the fundamental frequency of the harmonic signal increases proportionally, and peaks of the harmonic signal are at integer times of the fundamental frequency. For example, the fundamental frequency of the harmonic signal is 10.3 Hz; other dominant components with peaks in the power spectrum are integer multiples of about 10 Hz (19.8 Hz, 30.1 Hz, and 40.3 Hz) in the case of $N = 8$ at a sliding speed of 100 mm/s. These tendencies are the same for the N values are 4 and 6; the corresponding results are shown in **Figure S3** and **Figure S4** , respectively. For the design of the DPS and SPICE simulation, we chose an N value of 8 to maximize the energy conversion efficiency and to increase the frequency of the output signal; this was done to target the relatively slow sliding speed of 100 mm/s because mechanical motion in natural environments like ocean waves has an extremely low frequency, below 1 Hz. To investigate the effect of the sliding speeds and N values on the fundamental frequency, the fundamental frequencies in the FS-TENG were compared with different sliding speeds and N values. (**Figure S5**) The experimental results show that the fundamental frequency is linearly proportional to the sliding speeds and N values.

The operating principle of the DCC is shown in **Figure 3a** . The differential signal V_s generated by the FS-TENG is stored in capacitors C_{m1} and C_{m2} sequentially according to the direction of the electric current. For example, when V_s is a positive voltage, C_{m1} is charged and when V_s is a negative voltage, C_{m2} is charged. The electric charges stored inC_{m1} and C_{m2} are discharged over time by crossing through a switching operation using a MOSFET transistor. The proposed DCC matches the impedance between the FS-TENG and the load by cross-switching operation according to the current direction of V_s. The matched impedance Z_m is determined by the capacitances of the DCC, according to the following Equation (1):

$$Z_m = \frac{1}{2\pi f_1 C_m} \quad (1)$$

where f_1 is the fundamental frequency of V_s, and the capacitances of C_{m1} and C_{m2} are set equal to C_m. The supporting information explains the detailed method for determiningC_m of in terms of impedance matching using DCC and compares the proposed DCC with the conventional rectifier circuits as shown in**Figure S6 and S7** .

The CFC consists of a series of resistance and LC resonance circuits connected in parallel as shown in **Figure 3b** . The inductor and capacitor of the CFC block the high-frequency signal$V_{\mathrm{DCC}}(f_h)$ and the low-frequency signal$V_{\mathrm{DCC}}(f_l)$ and harvest the power of the resonance band signal $V_{\mathrm{DCC}}(f_{\mathrm{LC}})$. As a result, the CFC supplies a constant DC voltage to the electrical load by harvesting the power of the harmonic components supplied by the FS-TENG as shown in**Figure 3c** . The i-th resonant frequency $f_{LC(i)}$ of the CFC is given by following Equation (2):

$$f_{LC(i)} = \frac{1}{2\pi\sqrt{L_i C_i}} \quad (2)$$

where L_i and C_i are the inductance and capacitance of the$i$-th inductor and capacitor. The Q-factor Q_i and bandwidth$f_{LC(i)}$ of $f_{LC(i)}$ according to the resistance R, C_i and L_i are determined as following Equation (3) and (4), respectively:

$$Q_i = \frac{(2\pi f_{LC(i)})L_i}{R} \quad (3)$$

$$f_{LC(i)} = \frac{R}{2\pi L_i} \quad (4)$$

To resonate with a constant Q-factor at the fundamental and harmonic frequencies, the CFC is designed so that the capacitance of the i-th capacitor is set equal to C and L_i is set as following Equation (5):

$$L_i = \frac{1}{C(2\pi i f_1)^2} \quad , \; C_1 = C_2 = \cdots = C_I = C, \quad i = 1,\ 2,\ \cdots,\ I \quad (5)$$

where L_i is set so that the CFC resonates at f_1 and$i$-fold harmonic frequencies. The resonance bandwidth, which takes into account the frequency deviation of the signal generated by the FS-TENG, can be determined as R, as follows:

$$R \geq 2\pi n f_1 L_i \quad (6)$$

where f_1 is the fundamental frequency deviation of the FS-TENG.

For the SPICE simulation, we assume that the FS-TENG moves at a sliding speed of 100 mm/s. As shown in **Figure 2g** , f_1 andf_1 of the generated signal are 10 Hz and 0.6 Hz, respectively. The FS-TENG is equivalent to a circuit model with internal capacitanceC_0 and source V_0 connected in series.[34] The internal capacitance determined with an LCR meter, C_0, is found to be 72 pF. The internal impedance of the FS-TENG is calculated and found to be$1/2\pi f_1 C_0$= 221 MΩ. Next, the source voltage, V_0, can be estimated using a first-order inverse Butterworth filter on the measured voltage at 40 MΩ, as shown in **Figure S8** .[34]

We set C_m= 1.6 nF so that Z_m= 10 MΩ in Equation (1), and implemented MOSFET transistors of the DCC with Infineon's BSP92 and BUZ73AGE. **Figure 3d–e** show the voltage and spectrum loaded to 10 MΩ by DCC in the SPICE simulation. The DCC converts V_s to the ground-referenced voltage *via* double charging and cross-switching operation according to the direction of the electric current, as shown in **Figure 3d** . The signal converted by DCC includes the harmonic components of V_s, as shown in **Figure 3e** . The high-frequency component is reduced and the DC component is increased in the capacitor charging process. **Figure 3f** shows the average DCC power of single reciprocating motion of the FS-TENG compared to the bridge diode rectifier *via* SPICE simulation. The proposed DCC reduces the impedance of the FS-TENG from 221 MΩ to 11 MΩ and supplies 47.46 % higher power than that of the bridge diode rectifier. Due to the internal resistance of the MOSFET transistors, the impedance of 11 MΩ matched by DCC has an error of 1 MΩ compared to Z_m= 10 MΩ, calculated in Equation (1).

The CFC, which comprises four LC resonant circuits, is used to collect the power from the fundamental frequency and the 1st to 3rd harmonic frequencies generated by the FS-TENG. The design of the CFC is based onf_1 =10 Hz and f_1 = 1 Hz, as outlined in **Table 1** . Different design values were also investigated for Cases A, B, and C in**Table 1** using Equations (5) and (6) with different Cvalues. **Figure 3g** shows simulation results of the supply voltages to 10 MΩ of different CFCs according to Cases A, B, and C. The simulation results indicate that the CFCs provide a constant DC voltage of 2.09 V after the capacitor is fully charged, as illustrated in**Figure 3g** . Consequently, the CFC takes the shortest time of 0.89 hours to fully charge the capacitor for the DC voltage supply in Case C, where C is the smallest. However, achieving a

shorter charging time requires an increse in the physical size of the inductors due to the relationship between L_i and C as shown in Equation (5).

Figure S9 demonstrates that the proposed DPS can supplyK^2 times higher DC power using only a single CFC when FS-TENG and DCC are connected in K $\times$ K series. For verification of this, SPICE simulation was conducted by randomly changing the full-scale range of V_0 within $\pm$ 30 % for multiple signal sources of FS-TENG and adjusting the size within $\pm$ 10 % in units of samples.**Figure 3h** shows the DC output voltage of the DPS when 2 $\times$ 2 units of FS-TENG and DCC are utilized. It can be observed from the figure that the DPS using 2 $\times$ 2 units of FS-TENG and DCC supplies a DC voltage of 4.17 V, which is approximately twice as high as that obtained from a single unit. As a result, the power supplied to the load increases by approximately a factor of four as both voltage and current increase, although it takes the same time to reach the same voltage. In addition, when 10 $\times$ 10 units are used, **Figure 3i** demonstrates that a DC voltage of approximately 20.65 V is provided within a certain period depending on the C value.

The power evaluation of the proposed DPS is conducted in **Figure 4a and b** based on the number of LC circuits. The estimated power obtained from one to four harmonics is between 0.367 μW and 0.436 μW.**Figure 4c** shows that the power conversion efficiency of the DPS increases as the load current decreases and varies depending onC_m. Furthermore, we evaluate the efficiency of the DPS according to the load impedance and present the result in **Figure 4d** . To demonstrate high efficiency of the proposed DPS, a comparison between the proposed DPS and conventional buck converter and buck-boost converter circuits is performed by using SPICE simulation in**Figure S10.** The results clearly demonstrate that the proposed DPS can supply a sustainable DC output voltage and higher power with minimum ripple than the conventional converter circuits.

We implemented the DPS connected to the FS-TENG and verified the integrated system through experiments using the motorized linear stage, as shown in **Figure 5a and b** . For verification of the simulated results, the FS-TENG with an N value of 8 used for SPICE simulation was applied to the motorized linear stage at a sliding speed of 100 mm/s. The DCC was implemented with the same C_m and MOSFET transistors used in the SPICE simulation. The CFC was implemented using Case C shown in **Table 1** . The voltage supplied to the 10 MΩ load is shown in **Figure 5c and d** when the FS-TENG is moving at a speed of 100 mm/s. The converted ground-referenced voltage is shown in**Figure 5c** and a continuous 2.20 V DC voltage with 0.039 % ripple (0.87 mV_{pp}) was obtained for 0.54 hours of charging, as shown in **Figure 5d** .

For a practical application of the suggested FS-TENG and the DPS, we demonstrated a self-powered temperature sensor using a thermistor and data acquisition (DAQ) system. The operating processes are explained in the flow chart in **Figure 6a** . The FS-TENG generated an AC output voltage through sliding motion, which was then converted into a constant DC output voltage. The DPS supplied this constant DC output voltage to the thermistor module, which had a high impedance similar to the matched impedance after the DPS. (**Figure S11**) We used the thermistor to measure temperature based on the principle of change in resistance corresponding to temperature change. The self-powered temperature sensor was implemented by comparing the initial applied voltage supplied from the DPS with the voltage applied to the thremistor. We used a DAQ system and personal computer (PC) to collect voltage data across the thermistor and to estimate the temperature. The DPS played a critical role in providing a stable DC voltage with minimal fluctuations to the thermistor, enabling the demonstration of a self-powered sensor that can operate reliably in real-world applications.

Figure 6b depicts the experimental setup used to demonstrate the practical application of the FS-TENG and the DPS. We used a shape memory alloy (SMA) actuator, which reacts quickly and sensitively to temperature changes around the phase transition temperature, to visually confirm temperature changes. The SMA actuator had a phase transition temperature of approximately 50 °C and was heated using a commercial hair dryer. **Figure 6c** shows the experimental processes of the demonstration using the thermistor and SMA actuator. Initially, the SMA actuator was stretched due to gravitational force (i); however, it rapidly shrank and showed a high-temperature warning sign due to the phase transition when heated to 50 °C (ii). After heating stopped, the SMA actuator slowly returned to its initial stretched state (iii). (See**Video S1**) **Figure**

6d presents the results of temperature measurement *via* resistance changes in the thermistor and also provides a real-time temperature graph consistent with the aforementioned actuator deformation process. (See **Video S2**)

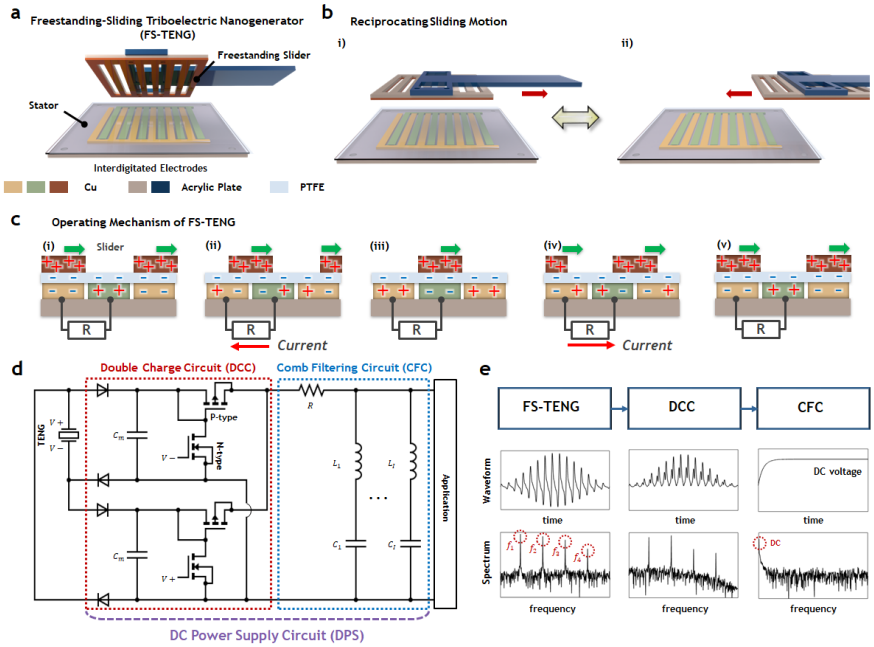

Figure 1. Schematic diagram and working mechanism of suggested DPS. (a) Schematic illustration and (b) reciprocating motion of FS-TENG. (c) Operating mechanism of FS-TENG in short-circuit condition. (d) Schematic circuit diagram of DPS. (e) Framework of DPS for FS-TENG.

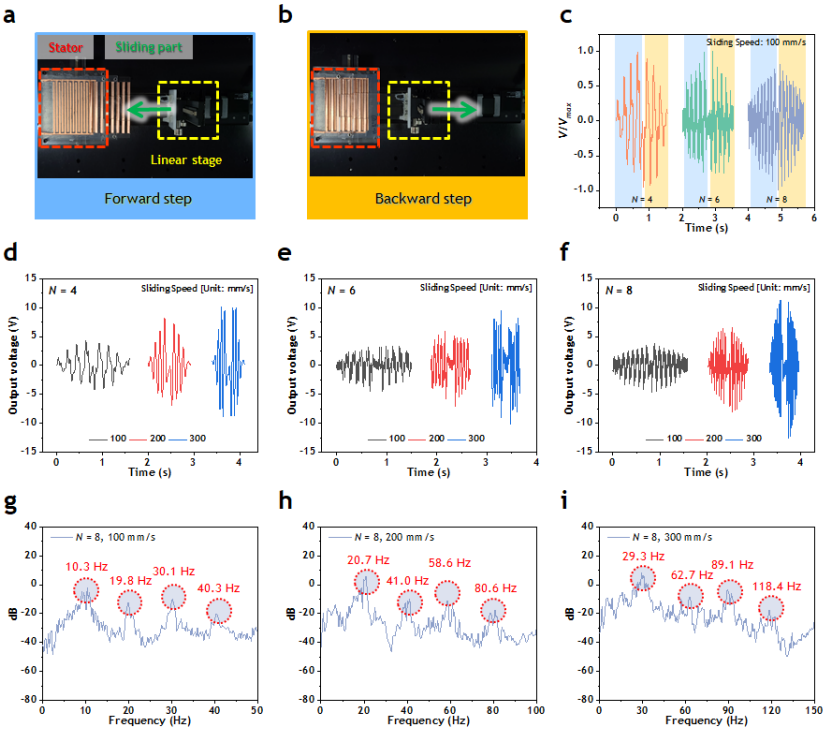

Figure 2. Electrical characterization of FS-TENG. Photographic image of (a) forward step and (b) backward step of FS-TENG using motorized linear stage. (c) Normalized voltages of FS-TENGs with different N values of 4, 6, and 8 at the same sliding speed of 100 mm/s. Output voltages of FS-TENGs at different sliding speeds of 100, 200, and 300 mm/s with different N values of (d) 4, (e) 6, and (f) 8. Power spectra of output voltage of FS-TENG with N value of 8 at sliding speeds of (g) 100 mm/s, (h) 200 mm/s, and (i) 300 mm/s, used to investigate harmonic frequency characteristics.

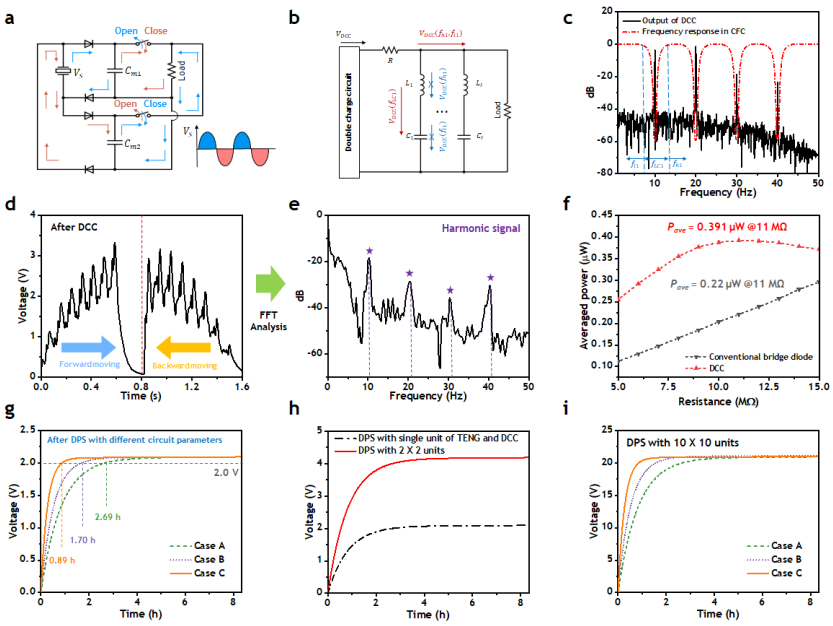

Figure 3. Working principle and SPICE simulation results of DPS. Working principles of (a) DCC and (b) CFC. (c) Output spectrum of DCC and frequency response of CFC. (d) Output voltage and (e) spectrum of DCC loaded to 10 MΩ. (f) Averaged power of DCC and bridge diode rectifier, (g) supply voltages of CFC according to RLC component values, (h) supply voltages of DPS with 2×2 units and single unit of FS-TENG and DCC, and (i) supply voltages of DPS with 10×10units of FS-TENG and DCC according to RLC component values of CFC.

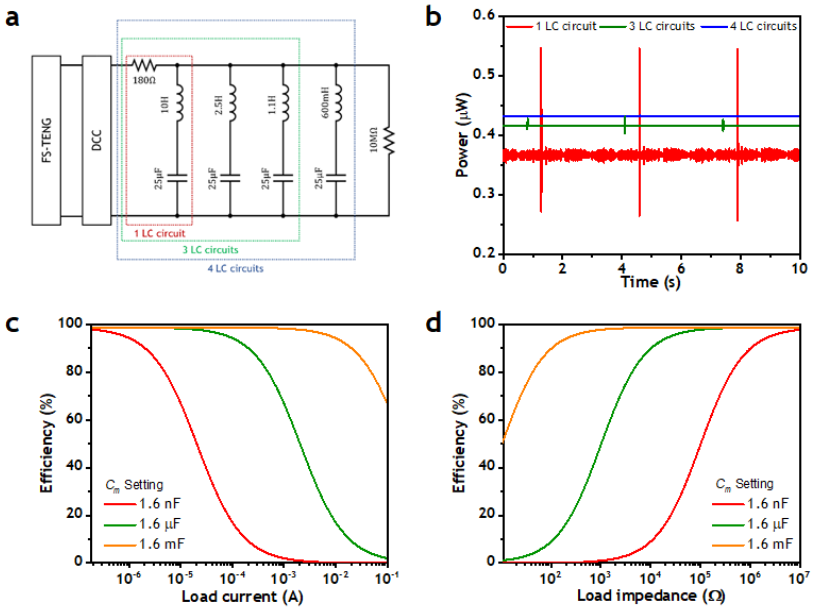

Figure 4. Supplied power and efficiency of DPS. (a) DPS circuit diagram for 10 MΩ load and (b) supplied

powers according to the number of harmonic tones. Efficiency of the DPS with different capacitances according to (c) load current and (d) load impedance.

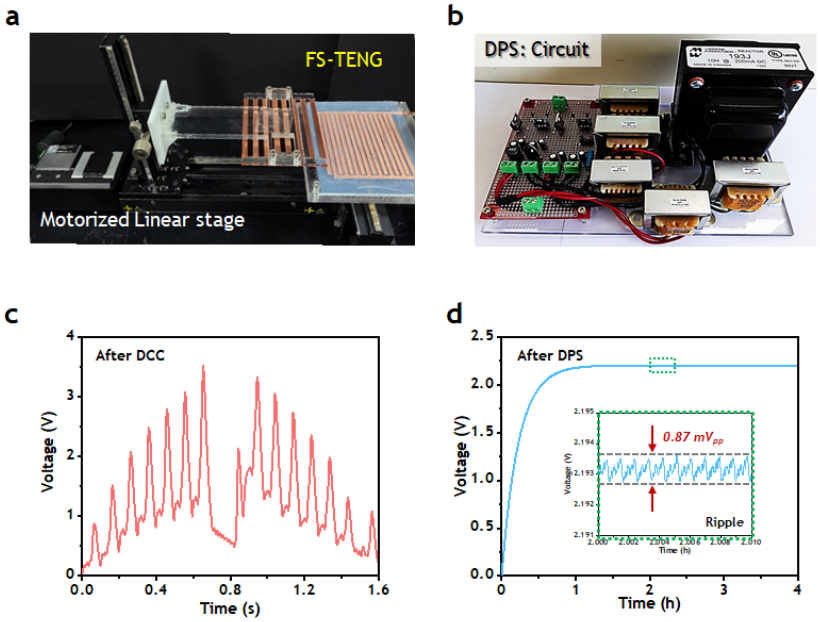

Figure 5. Experimental verification of DSP. Photographic images of (a) FS-TENG and (b) circuit part of DPS. Output voltages of (c) DCC and (d) DPS (inset: magnified graph of constant voltage output with ripple).

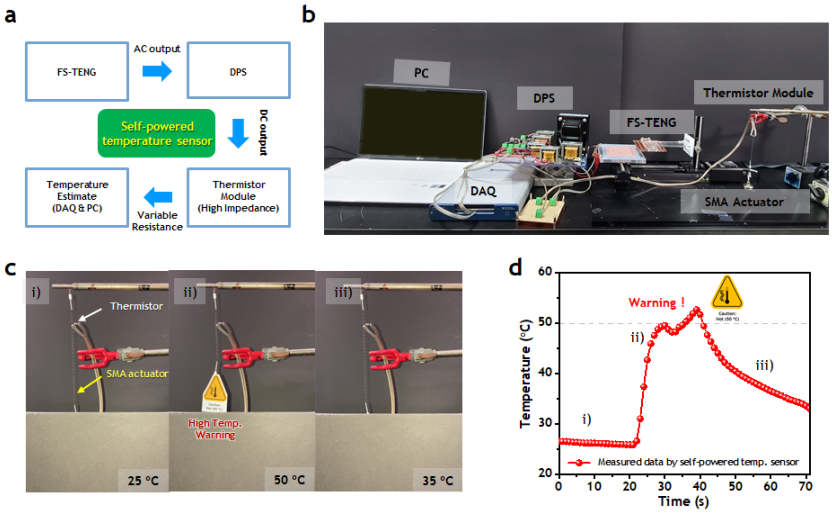

Figure 6. Practical application of real-time and wireless self-powered temperature sensor. (a) Operating processes of real-time wireless self-powered temperature sensor and (b) experimental setup for operating real-time wireless self-powered temperature sensor and SMA actuator. (c) Photographic images of thermistor module and SMA actuator at each temperature stage: i) room temperature (25 °C), ii) 50 °C, and iii) 35 °C. (d) Temperature graph measured by self-powered thermistor module.

3. Conclusion

In this study, we developed a DPS circuit suitable for FS-TENGs with high internal impedance and multiple harmonic output signals. To properly resolve the high internal impedance of the FS-TENG, measured as 221 MΩ, the DCC composed of capacitors and MOSFET transistors was used as a rectifier circuit. In addition, the DCC played a critical role to match the impedance between the FS-TENG and the load by cross-switching operation from 221 MΩ to 11 MΩ. The output electrical signals of the FS-TENGs have multiple harmonic components and therefore a lot of electrical energy will be wasted in energy harvesting circuits if high-order harmonic terms will not be considered. Therefore, the CFC, which consists of multiple RLC resonators, was implemented to collect the wasted energy of higher-order harmonic terms. Electrical characterization of the FS-TENG was conducted to investigate the output frequency characteristics and effects of the sliding speed and number of segments on the frequency and magnitude of the output voltage. Eventually, the FS-TENG integrated with DPS can supply a stable DC voltage to the load by successfully harvesting the power from the multiple harmonic output signals generated by the FS-TENG. The present results show that the suggested FS-TENG and DPS can supply a continuous DC voltage of 2.2 V to loads and reduce the FS-TENG impedance from 221 MΩ to 11 MΩ, simultaneously. Notably, this work provides a DC output power of 2.2 V at a sliding frequency of 0.625 Hz. The suggested DPS can pave the way for the development of next-generation renewable energy harvesters using AC/DC converting circuits to supply sustainable and stable electrical energy to future practical electronic applications.

4. Material and Methods

4.1. Fabrication of FS-TENG

The FS-TENG comprises a stator with interdigitated electrodes and a grating slider. The acrylic substrates used to fabricate the stator and slider part were cut and engraved by a laser cutting machine (Coryart, C40). Copper film (Goodfellow, CU000420, Purity: 99.95%) was attached to the engraved substrate for the stator and cut into interdigitated shapes with different N values. For triboelectrification, a PTFE film with a thickness of 0.08 mm was attached to the top side of the interdigitated copper electrodes for the contact surfaces of the stator part. The grating-shaped acrylic substrate of the slider part was also cut by the laser cutting machine, and the copper film was attached to the substrate as an electropositive contact material of the FS-TENG.

4.2. Electrical characterization of FS-TENG

To investigate the output characteristics of the FS-TENG, electrical characterization was conducted using a motorized linear stage (Zaber, X-LSQ150D) to control the sliding speed and linear displacement. A digital phosphor oscilloscope (Tektronix, DPO 2002B) and a high-voltage probe with an internal impedance of 40 M were used to measure the output voltage of the FS-TENG.

4.3. Demonstration of real-time wireless self-powered temperature sensor

Nitinol SMA wire (PEIERTECH, MFWT00350CS11-01) with a transition temperature of 48 °C and a diameter of 350 μm, was coiled into spring form used for the SMA actuator. A commercially available hair dryer was utilized to heat the SMA actuator and thermistor module to 50 °C. The thermistor module for temperature measurement was implemented by connecting a 505YG7K thermistor (Littelfuse) and a 5 MΩ resistor in series, as shown in **Figure S11** . The output voltageV_{th} of the thermistor module was digitized by the DAQ device(USB-6351, National Instruments). The Labview-based graphical user interface (GUI) software was used to convert V_{th} to a temperature value in real time.

Supporting Information

Supporting Information is available from the Wiley Online Library or from the author.

Acknowledgements

Funding: This work was supported by Creative Research Initiative Program (2015R1A3A2028975) funded

by National Research Foundation of Korea (NRF), and the Defense Acquisition Program and the Agency for Defense Development (ADD) in Korea under the contract UD200011DD.

Author contributions: K. Lee and J.-S. Kim contributed equally to this work. K. Lee, J.-S. Kim, I.-K. Oh, and C. H. Lee conceived the idea of a DC power supply circuit. K. Lee and J.-S. Kim conducted all experiments and wrote the manuscript. S. Oh and H. Yoo contributed to data analyses. J. Lee, I.-K. Oh, and C. H. Lee achieved the funding for this project. I.-K.Oh and C. H. Lee supervised the research at all stages, led all groups, and wrote the manuscript. All authors discussed the results and commented on the manuscript.

Received: (will be filled in by the editorial staff) Revised: (will be filled in by the editorial staff) Published online: (will be filled in by the editorial staff)

References

[1] S. Chu, A. Majumdar, *Nature* , **2012** , 488, 294-303.

[2] S. Sen, S. Ganguly, *Renew. Sustain. Energy Rev.* ,**2017** , 69, 1170-1181.

[3] V. Annapureddy, H. Palneedi, G.-T. Hwang, M. Peddigari, D.-Y. Jeong, W.-H. Yoon, K.-H. Kim, J. Ryu, *Sustain. Energy Fuels* ,**2017** , 1, 2039-2052.

[4] Y. Mao, D. Geng, E. Liang, X. Wang, *Nano Energy* ,**2015** , 15, 227-234.

[5] C. Wu, A.C. Wang, W. Ding, H. Guo, Z.L. Wang, *Adv. Energy Mater.* , **2019** , 90, 1802906.

[6] Z.L. Wang, *Adv. Energy Mater.* , **2020** , 10, 2000137.

[7] A. Ahmed, I. Hassan, M.F. El-Kady, A. Radhi, C.K. Jeong, P.R. Selvaganapathy, J. Zu, S. Ren, Q. Wang, R.B. Kaner, *Adv. Sci.* ,**2019** , 6, 1802230.

[8] Z.L. Wang, T. Jiang, L. Xu, *Nano Energy* , **2017** , 39, 9-23.

[9] M. Ma, Z. Kang, Q. Liao, Q. Zhang, F. Gao, X. Zhao, Z. Zhang, Y. Zhang, *Nano Res.* , **2018** , 11, 2951-2969.

[10] S. Niu, Z.L. Wang, *Nano Energy* , **2015** , 14, 161-192.

[11] W. Liu, Z. Wang, C. Hu, *Mater. Today* , **2021** , 45, 93-119.

[12] J. Chung, D. Heo, G. Shin, D. Choi, K. Choi, D. Kim, S. Lee,*Adv. Energy Mater.* , **2019** , 9, 1901731.

[13] Z. Yang, Y. Yang, H. Wang, F. Liu, Y. Lu, L. Ji, Z.L. Wang, J. Cheng, *Adv. Energy Mater.* , **2021** , 11, 2101147.

[14] A.R. Mule, B. Dudem, H. Patnam, S.A. Graham, J.S. Yu, *ACS Sustain. Chem. Eng.* , **2019** , 7, 16450-16458.

[15] J.-S. Kim, J. Kim, J.-N. Kim, J. Ahn, J.-H. Jeong, I. Park, D. Kim, I.-K. Oh, *Adv. Energy Mater.* , **2022** , 12, 2103076.

[16] S. Wang, Y. Xie, S. Niu, L. Lin, Z.L. Wang, *Adv. Mater.* ,**2014** , 26, 2818-2824.

[17] S. Niu, Y. Liu, X. Chen, S. Wang, Y.S. Zhou, L. Lin, Y. Xie, Z.L. Wang, *Nano Energy* , **2015** , 12, 760-774.

[18] Q. Tang, X. Pu, Q. Zeng, H. Yang, J. Li, Y. Wu, H. Guo, Z. Huang, C. Hu, *Nano Energy* , **2019** , 66, 104087.

[19] Y. Xie, S. Wang, S. Niu, L. Lin, Q. Jing, J. Yang, Z. Wu, Z.L. Wang, *Adv. Mater.* , **2014** , 26, 6599-6607.

[20] D. Zhang, J. Shi, Y. Si, T. Li, *Nano Energy* ,**2019** , 61, 132-140.

[21] B. Kil Yun, H. Soo Kim, Y. Joon Ko, G. Murillo, J. Hoon Jung,*Nano Energy* , **2017** , 36, 233-240.

[22] Z. Wen, H. Guo, Y. Zi, M.-H. Yeh, X. Wang, J. Deng, J. Wang, S. Li, C. Hu, L. Zhu, Z.L. Wang, *ACS Nano* , **2016** , 10, 6526-6534.

[23] L. Yin, K.N. Kim, J. Lv, F. Tehrani, M. Lin, Z. Lin, J.-M. Moon, J. Ma, J. Yu, S. Xu, J. Wang, *Nat. Commun.* , **2021** , 12, 1542.

[24] Y. Song, J. Min, Y. Yu, H. Wang, Y. Yang, H. Zhang, W. Gao,*Sci. Adv.* , **2020** , 6, eaay9842.

[25] W. Tang, T. Zhou, C. Zhang, F. Ru Fan, C. Bao Han, Z. Lin Wang,*Nanotechnology* , **2014** , 25, 225402.

[26] Y. Zi, H. Guo, J. Wang, Z. Wen, S. Li, C. Hu, Z.L. Wang,*Nano Energy* , **2017** , 31, 302-310.

[27] J. Ahn, J.-S. Kim, Y. Jeong, S. Hwang, H. Yoo, Y. Jeong, J. Gu, M. Mahato, J. Ko, S. Jeon, J.-H. Ha, H.-S. Seo, J. Choi, M. Kang, C. Han, Y. Cho, C.H. Lee, J.-H. Jeong, I.-K. Oh, I. Park, *Adv. Energy Mater.* , **2022** , 12, 2201341.

[28] X. Liang, T. Jiang, Y. Feng, P. Lu, J. An, Z.L. Wang,*Adv. Energy Mater.* , **2020** , 10, 2002123.

[29] G. Zhu, J. Chen, T. Zhang, Q. Jing, Z.L. Wang, *Nat. Commun.* , **2014** , 5, 3426.

[30] F. Xi, Y. Pang, W. Li, T. Jiang, L. Zhang, T. Guo, G. Liu, C. Zhang, Z.L. Wang, *Nano Energy* , **2017** , 37, 168-176.

[31] A. Chandrasekhar, N.R. Alluri, M.S.P. Sudhakaran, Y.S. Mok, S.-J. Kim, *Nanoscale* , **2017** , 9, 9818-9824.

[32] K.-W. Han, J.-N. Kim, A. Rajabi-Abhari, V.-T. Bui, J.-S. Kim, D. Choi, I.-K. Oh, *Adv. Energy Mater.* , **2021** , 11, 2002929.

[33] Y. Gai, Y. Bai, Y. Cao, E. Wang, J. Xue, X. Qu, Z. Liu, D. Luo, Z. Li, *Small* , **2022** , 18, 2108091.

[34] J. Lee, J. Ahn, H. Jin, C.H. Lee, Y. Jeong, K. Lee, H.-S. Seo, Y. Cho, *Micromachines* , **2022** , 13, 579.

Table 1. RLC component values of CFC.

Case A.	$R = 180\Omega$, $C = 90\mu\Phi$, $L_1 = 3H$ $L_2 = 700mH$ $L_3 = 310mH$ $L_4 = 180mH$
Case B.	$R = 300\Omega$, $C = 50\mu\Phi$, $L_1 = 5H$ $L_2 = 1.25H$ $L_3 = 560mH$ $L_4 = 300mH$
Case C.	$R = 600\Omega$, $C = 25\mu\Phi$, $L_1 = 10H$ $L_2 = 2.5H$ $L_3 = 1.1H$ $L_4 = 600mH$